NANO LETTERS

Cite This: Nano Lett. XXXX, XXX, XXX−XXX

Letter

pubs.acs.org/NanoLett

Theoretical Calculation Guided Design of Single-Atom Catalysts toward Fast Kinetic and Long-Life Li−S Batteries

Guangmin Zhou,[†,‡,◆] Shiyong Zhao,[§,◆] Tianshuai Wang,[∥,◆] Shi-Ze Yang,[⊥] Bernt Johannessen,[#] Hao Chen,[†] Chenwei Liu,[†] Yusheng Ye,[†] Yecun Wu,[†] Yucan Peng,[†] Chang Liu,[∇] San Ping Jiang,*[§] Qianfan Zhang,*[∥] and Yi Cui*[†,○]

†Department of Materials Science and Engineering, Stanford University, Stanford, California 94305, United States

‡Shenzhen Geim Graphene Center, Tsinghua-Berkeley Shenzhen Institute, and Tsinghua Shenzhen International Graduate School, Tsinghua University, Shenzhen 518055, China

§Fuels and Energy Technology Institute and WA School of Mines: Minerals, Energy, and Chemical Engineering, Curtin University, Perth, Western Australia 6102, Australia

∥School of Materials Science and Engineering, Beihang University, Beijing, 100191, P.R. China

⊥Materials Science and Technology Division, Oak Ridge National Laboratory, Oak Ridge, 37831, United States

#Australian Synchrotron, Clayton, Victoria 3168, Australia

∇Advanced Carbon Division, Shenyang National Laboratory for Materials Science, Institute of Metal Research, Chinese Academy of Sciences, Shenyang, Liaoning 110016, China

○Stanford Institute for Materials and Energy Sciences, SLAC National Accelerator Laboratory, 2575 Sand Hill Road, Menlo Park, California 94025, United States

S Supporting Information

ABSTRACT: Lithium−sulfur (Li−S) batteries are promising next-generation energy storage technologies due to their high theoretical energy density, environmental friendliness, and low cost. However, low conductivity of sulfur species, dissolution of polysulfides, poor conversion from sulfur reduction, and lithium sulfide (Li2S) oxidation reactions during discharge−charge processes hinder their practical applications. Herein, under the guidance of density functional theory calculations,

we have successfully synthesized large-scale single atom vanadium catalysts seeded on graphene to achieve high sulfur content (80 wt % sulfur), fast kinetic (a capacity of 645 mAh g^{-1} at 3 C rate), and long-life Li−S batteries. Both forward (sulfur reduction) and reverse reactions (Li2S oxidation) are significantly improved by the single atom catalysts. This finding is confirmed by experimental results and consistent with theoretical calculations. The ability of single metal atoms to effectively trap the dissolved lithium polysulfides (LiPSs) and catalytically convert the LiPSs/Li2S during cycling significantly improved sulfur utilization, rate capability, and cycling life. Our work demonstrates an efficient design pathway for single atom catalysts and provides solutions for the development of high energy/power density Li−S batteries.

KEYWORDS: Single-atom catalysts, lithium−sulfur batteries, catalytic conversion, graphene, density functional theory simulation
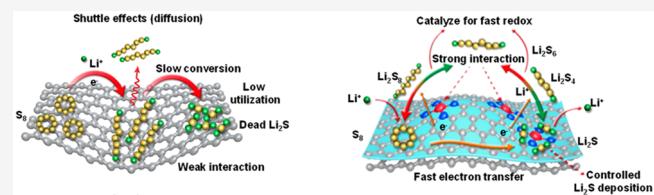
Lithium−sulfur (Li−S) battery is regarded as a promising candidate for energy storage due to its high energy density, low cost, and environmental friendliness.[1−3] Nevertheless, technological challenges arising from the low electronic/ionic conductivity of sulfur species, the sluggish reaction kinetics with accumulated sulfur species, and dissolved polysulfides, lead to large internal resistance, low sulfur utilization, and fast capacity decay.[4−6] These challenges have prevented the commercialization of Li−S batteries. To overcome these drawbacks, introducing active adsorption and catalysis centers is required for the cathode to enhance the sulfur utilization and accelerate the reversible conversion between lithium polysulfides (LiPSs) and Li2S. Therefore, much effort has been devoted to developing highly active and durable catalysts,

which possess well-designed activation centers capable of adsorbing active species and facilitating desired redox reactions.[7−10] Our previous work identified metal sulfides as effective catalysts in lowering the overpotential and the Li2S decomposition energy barrier compared with the more commonly used carbon materials in Li−S batteries.[11] Several other bulk and nanosized catalysts including TiO$_{2−x}$ nanosheets,[10] MnO2 nanosheets,[12] Fe2O3 nanoparticles,[13] mesoporous TiN,[14] amorphous CoS3 film,[15] VN nanoribbon,[16] and
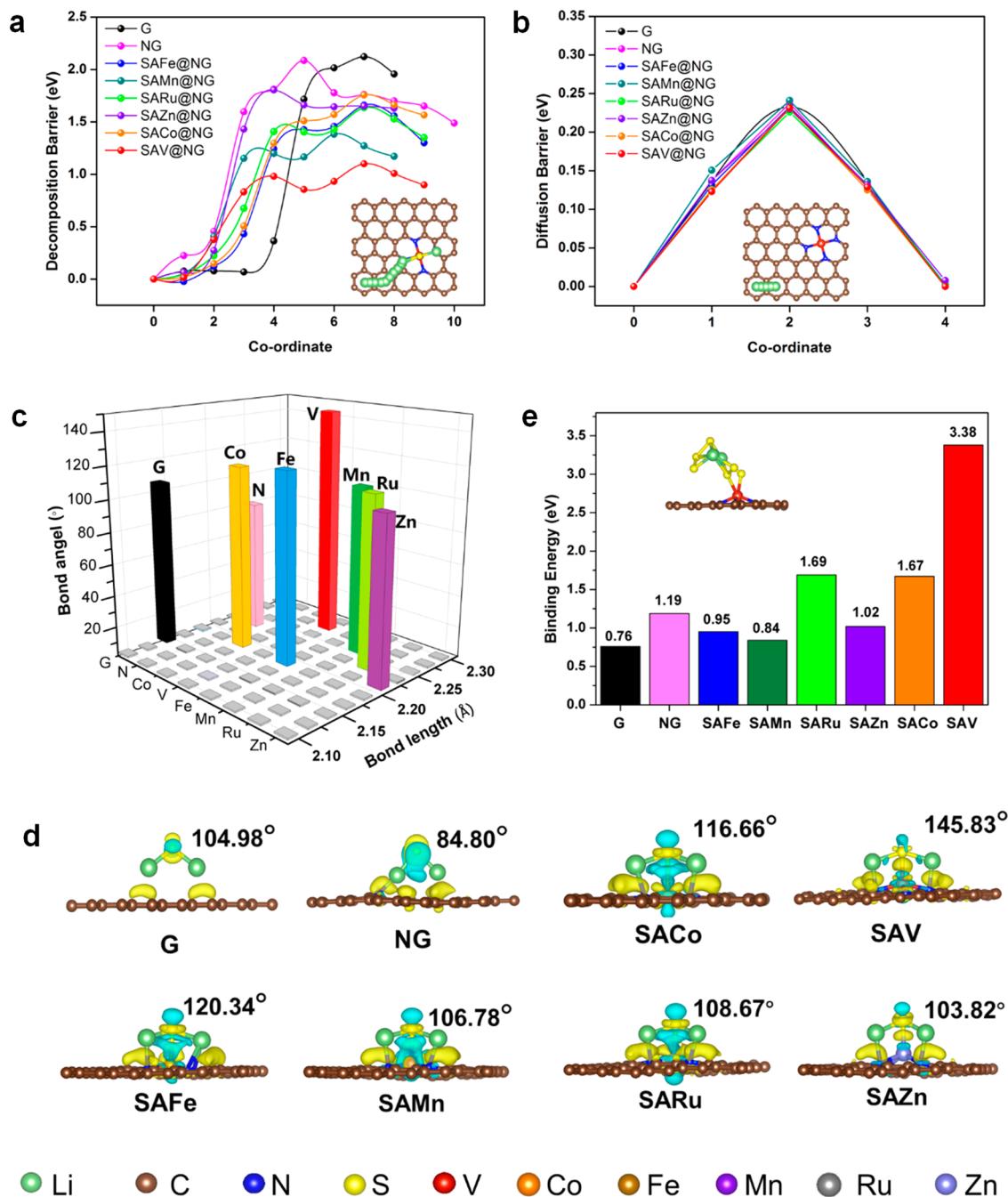
Figure 1. Theoretical understanding for Li$_2$S decomposition, Li ion diffusion, and anchoring effect. (a) Decomposition barriers of Li$_2$S and (b) lithium ion diffusion barriers on different substrates including graphene, NG, SAFe@NG, SAMn@NG, SARu@NG, SAZn@NG, SACo@NG, and SAV@NG. The inset images in panels a and b are the detailed decomposition path of Li$_2$S and diffusion pathway of lithium atom on SAV@NG, respectively. (c) Bond angle (Li—S—Li) of Li$_2$S, bond length (Li—S) of Li$_2$S and (d) side view for charge density difference of Li$_2$S adsorption on the graphene, NG, SACo@NG, SAV@NG, SAFe@NG, SAMn@NG, SARu@NG, and SAZn@NG, respectively. The yellow and blue sections represent the electron accumulate and lose region. The iso-surface is set to 0.003 eV/Å^3. (e) Binding energy of Li$_2$S$_6$ on the graphene, NG, SACo@NG, SAV@NG, SAFe@NG, SAMn@NG, SARu@NG, and SAZn@NG, respectively. The inset image is the side view for the Li$_2$S$_6$ cluster adsorption configurations on SAV@NG.

phosphorene[17] have also been synthesized to promote the transformation of sulfur, LiPSs, and Li$_2$S, resulting in a significant increase in utilization of active materials and enhancing the reaction kinetics of Li−S batteries.[8] However, attention should be paid to control the weight percentages of these inactive additives without sacrificing the overall energy density of Li−S batteries.

Since catalytic performance is correlated to catalytic particle size, it is natural to hypothesize that maximum catalytic efficiency is achieved at the single atomic level.[18−20] Single-atom catalysts (SACs), comprised of monodispersed single atoms supported on various substrates, have recently been demonstrated to exhibit high efficiency and distinctive selectivity in various energy, environment, and chemical-related devices, far exceeding conventional metal nanoparticle

catalysts.[21−23] SACs not only maximize the atomic efficiency, making every atom contribute, but also supply an alternative strategy to adjust the activity and selectivity of a catalytic process by introducing the lowest amount of catalyst.[19,21,24] Most recently, SACs have been studied and applied as electrocatalysts for Li−S batteries with significantly improved electrochemical performance.[25−28] However, in those studies SACs were randomly selected and fabricated via an impregnation method (relying on absorption sites of the substrates), which inherently limits variety and yield. To efficiently meet the requirements of Li−S batteries, both enhanced selection and synthesis sophistication are required.

Theoretical modeling represents a powerful tool to accelerate the search for promising catalyst candidates, which can significantly reduce the number of unsuccessful trials.[29,30] Taking the above discussion into consideration, herein we first screen SAC materials for the catalytic decomposition of Li_2S using theoretical simulation. Considering the cost issue and the diversity of metal atoms, 10 materials composed of graphene, N-doped graphene (NG), single atom Fe, Mn, Ru, Zn, Co, Cu, V, and Ag on NG were chosen. Among all the materials screened, we discover that vanadium single atoms on NG (SAV@NG) show the smallest decomposition barrier (1.10 eV). To apply SAV@NG as effective and practical cathodes for Li−S batteries, we develop one universal strategy, referred to as one seeding approach,[31] to synthesize single atoms coated on graphene with scalable quantities, controllable loading, and adjustable components. The results demonstrate a dramatic enhancement of capacity, kinetics, and cycling performance for SAV@NG-based electrodes in Li−S batteries, which is consistent with the simulation results.

Results and Discussion. First, the stability of these 10 materials (graphene, NG, SAFe@NG, SAMn@NG, SARu@NG, SAZn@NG, SACo@NG, SAV@NG, SACu@NG, and SAAg@NG) were considered. According to the optimized structure results, graphene, NG, and single atom substrates (Fe, Mn, Ru, Zn, Co, and V) can maintain pristine atomic configuration after the Li_2S and LiS adsorption, while the pristine substrates show a deformed atomic lattice after LiS cluster adsorption for the SACu@NG and SAAg@NG materials, that is, the pristine bonds between the Cu atom and adjacent coordinated N atoms break and Ag is replaced by the Li atom of LiS cluster (Figure S1a,b,j,k). The implication of this finding is that the single atom substrates (Fe, Mn, Ru, Zn, Co. and V) materials can maintain the structure stability during repeated charge−discharge cycles while the SACu@NG and SAAg@NG are unstable. We also calculate out that the decomposition energy barrier of Li_2S on these stable substrates was highly related to the kinetic property of Li_2S oxidation during the charging process. Reducing the decomposition barrier of Li_2S can greatly increase the utilization of active materials, decrease the formation of dead Li_2S, and achieve a long cycling life. We considered the decomposition process from an intact Li_2S molecule into a LiS cluster and a single Li ion, which corresponds to the breaking of the Li−S bond. The decomposition pathway of Li_2S on different substrates are shown in Figure 1a (inset for SAV@NG) and Figure S1c−i. The results show that graphene possesses the greatest decomposition barrier (2.12 eV), much larger than the other seven cases. The decomposition barrier for SAV@NG, SACo@NG, SAFe@NG, SAMn@NG, SARu@NG, and SAZn@NG are 1.10, 1.76, 1.66, 1.38, 1.64, and 1.81 eV, respectively. Meanwhile, the lithium ion diffusion properties on the

substrates were also important for studying the Li_2S decomposition performance. Fast lithium ion diffusion behavior facilitates the subsequent steps after the decomposition of Li_2S on the charging process and sulfur transformation chemistry on the discharging process. As shown in Figure 1b, the calculation results show that the diffusion barriers of lithium ion on all the substrates are around 0.23 eV. The detailed lithium diffusion pathway on these substrates are shown in the inset of Figure 1b (SAV@NG) and Figure S2. Combining the decomposition energy barriers of Li_2S with lithium ion diffusion barriers on these substrates, it can be clearly seen that the dominant step for the decomposition process of Li_2S on the charging process is the bond breaking step between the Li and S atoms. SAV@NG exhibits the smallest decomposition barrier (1.10 eV) of Li_2S and can maintain the small lithium diffusion barrier, which shows the best potential for catalyzing the decomposition of Li_2S.

To further have an in-deep investigation for the different catalytic effect on decomposition of Li_2S on these substrates, the electronic structure and thermodynamic configuration analysis were performed. Considering that the bond length (Li—S) and bond angle (Li—S—Li) can reflect the bonding strength of the Li—S bond in the Li_2S, we measured the bond length and angle of Li_2S after it was adsorbed on the substrates. As shown in Figure 1c and Figure S3, the bond length of Li—S on the graphene is the shortest with 2.15 Å and the bond angle of Li—S—Li on the NG is the smallest with 84.80°, while SAV@NG substrate possesses both a maximum bond length (2.28 Å, Li—S) and a maximum bond angle (145.83°, Li—S—Li) among all substrates. The longer bond length and bigger bond angle of Li_2S on relative substrates mean the greater weakening of the Li—S bond in the Li_2S molecules, which facilitate the decomposition of Li_2S. These results are in agreement with our decomposition barrier calculation. Moreover, electronic transformation behavior between the Li_2S and substrates were also considered. As shown in Figure 1d, the charge density differences show the electron migration mainly accumulates between the Li atoms and substrates for the graphene and NG materials. For the single atom substrates, in addition to the electron transfer between the Li atoms and substrates, it can be clearly seen that there is also more electron transfer between the S atom and the metal atoms, which can further weaken the Li—S bond by forming the S—metal bond and thus, decrease the decomposition barriers of Li_2S.

Besides, the interaction between the polysulfides and substrates was also considered. Previous works have identified that the stronger chemical interaction between the substrates and polysulfides can effectively decrease the shuttle effect.[32] As shown in Figure 1e and Figure S4, the binding energy, E_b, is computed to measure the binding strength between Li_2S_6 on these substrates. The binding energy is defined as $E_b = E_{Li2S6}$ (pure Li_2S_6 cluster) + E_{Sub} (pure substrate) − $E_{Li2S6+sub}$ (adsorbed system), while the positive and the larger value means the stronger anchoring effect of Li_2S_6 on the substrates. On the basis of the calculation results, the binding energy of Li_2S_6 on graphene, NG, SACo@NG, SAV@NG, SAFe@NG, SAMn@NG, SARu@NG, and SAZn@NG are 0.76, 1.19, 1.67, 3.38, 0.95, 0.84, 1.69, and 1.02 eV, respectively. The graphene exhibits the weakest chemical binding energy of 0.76 eV to Li_2S_6, while the NG and all of the single atom substrates can induce the bonding effect by N—Li or metal—S to increase the binding strength. Due to the direct bonding effect between the two S atoms of Li_2S_6 cluster and the V atoms (inset of
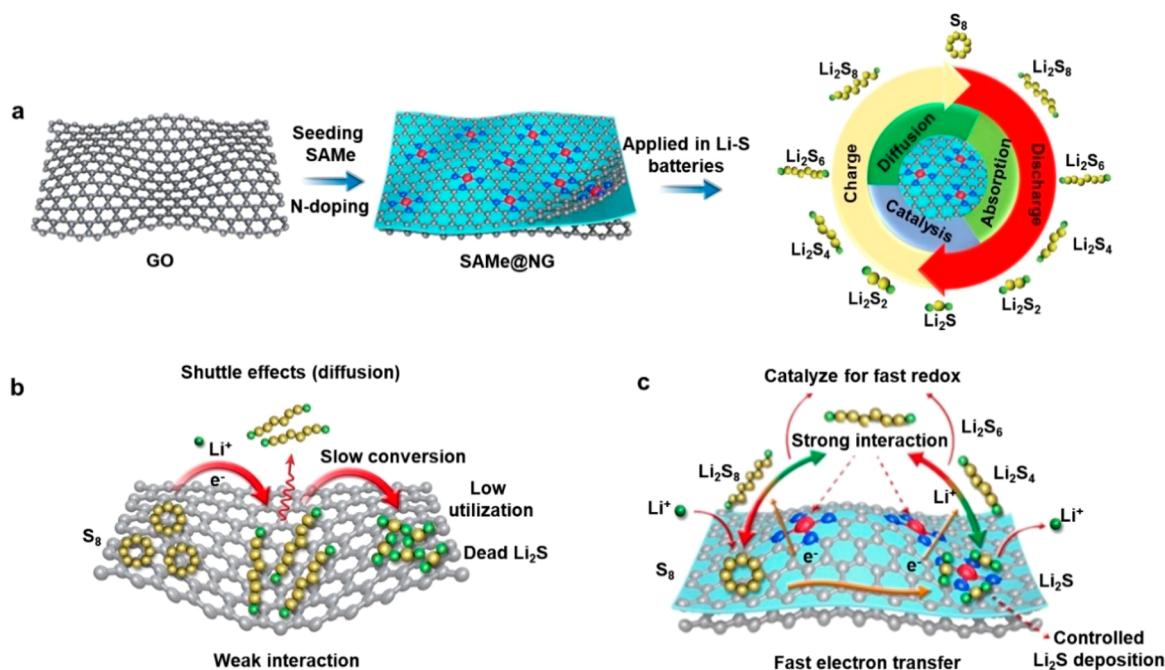
Figure 2. (a) Schematics showing the seeding approach of a single atom on graphene, the conversion process on (b) graphene, and (c) single atom seeded graphene for Li−S batteries.

Figure 1e), the SAV@NG substrate possesses the biggest binding energy of 3.38 eV. This indicates that the SAV@NG material exhibits the best potential on mitigating polysulfide dissolution and suppressing shuttle effect in Li−S batteries. Combining the decomposition barrier, lithium ion diffusion barrier, structure stability performance, and anchoring effect of the 10 materials, the SAV@NG shows the best potential and was thus selected as an optimum catalyst for this study. Moreover, according to the different decomposition energy barrier gradients of Li_2S, similar lithium ion diffusion barrier and different anchor effect level for Li_2S_6 on these substrates, graphene, NG, and SACo@NG were also selected as the control electrodes.

Guided by the theoretical results, a seeding approach was proposed to synthesize the SACo@NG and SAV@NG samples, as shown in Figure 2a. Briefly, the seeding approach involves three steps, that is, the seed of single atom metal (Seed-SAMe) preparation, graphene surface modification, and final seed landing (see Chart S1 and experimental details in Supporting Information). The surface modification layer was introduced on the surface of graphene oxide (GO), which bridged the connection between the GO and single atoms. The loading of seeds was controlled through absorbing and stabilizing the metal salts on the carbon nitrides. The components of the single atoms could be adjusted by changing the metal salts. Besides this, the content and loading were also adjustable through changing the ratio between the seeds and supports. Finally, the specific loading of single atom seeds was tested by inductively coupled plasma-optical emission spectroscopy (ICP-OES) and then was added into the mixture based on the targeted design. The seeds were almost completely decomposed during the annealing process and then the single atom metal was bonded with the GO support. For instance, Seed-SACo and Seed-SAV were successfully synthesized through changing appropriate metal salts and controlling the content. Furthermore, they were uniformly mixed with GO separately, followed by annealing treatments

prior to the final single atom samples. GO hinders the aggregation of Seed-SAMe into nanoparticles and provides abundant sites for the seed landing on the surface and then strongly bonds with GO. Benefiting from advantages of the single atom in the aspects of absorption, catalysis, and diffusion, the SAMe@NG-based electrodes show great promise in Li−S batteries during charge−discharge processes (Figure 2a. Generally, due to weak interaction between graphene and LiPSs along with a slow conversion process, the shuttle effects cannot be refrained and there are dead Li_2S agglomerates during the cycling (Figure 2b), resulting in a rapid capacity fading and low sulfur utilization. On the contrary, the multifunctional SACs can integrate the advantages of strong chemical adsorption of LiPSs, facilitated conversion among sulfur/lithium polysulfides/Li_2S, and controllable Li_2S deposition sites (Figure 2c), which promote the realization of high capacity, fast kinetics, and long-life Li−S batteries.

The SAV@NG and SACo@NG were prepared and scaled up as shown in the inset of Figure 3a, allowing for significant commercial potential. The mass loading of vanadium and cobalt of SAV@NG and SACo@NG prepared was characterized by thermogravimetric analysis (TGA) and further confirmed by ICP-OES with values of around 4.3 and 3.9 wt %, respectively (Figure S5a,b). The oxidation resistance temperature of NG, SACo@NG, and SAV@ NG are 558 °C, 500 °C, and 450 °C, respectively (Figure S5), and the reduced temperature indicates the catalytic effect of single atoms on the decomposition of NG. Scanning electron microscopy (SEM) and transmission electron microscopy (TEM) images of SAV@NG and SACo@NG demonstrate curved graphene without nanoparticles observed on the surface (Figure 3a,b and Figure S6a,b). X-ray diffraction (XRD) patterns further confirm that there are no metallic vanadium or oxide nanoparticles detectable in the products (Figure S7a), consistent with the TEM observations. Raman spectra indicate a similar ratio of D and G band, which means the amorphous carbon derived from polyvinylpyrrolid (PVP) and polyethyle-
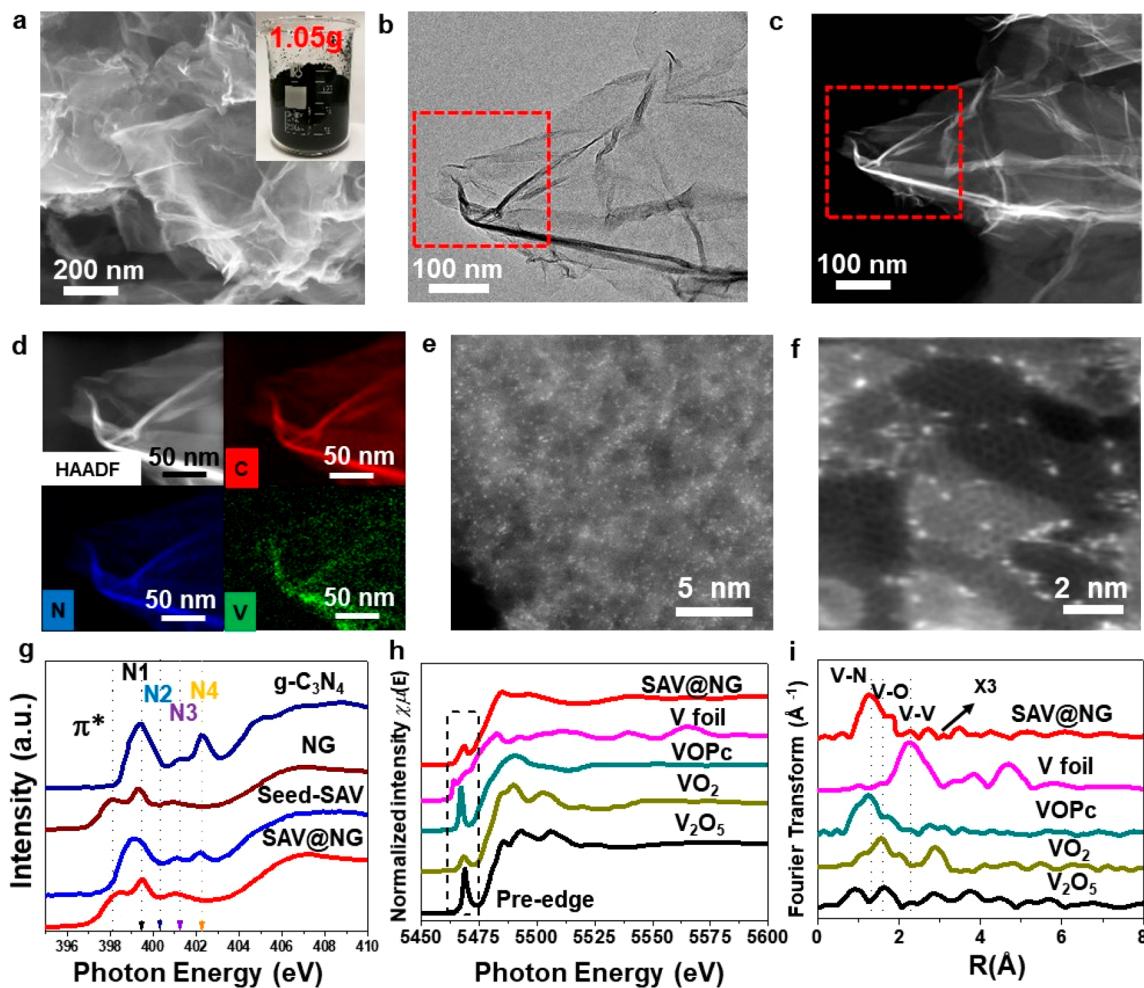
Figure 3. Structural characterizations of SAV@NG. (a) SEM image of SAV@NG, inset image: 1.05 g SAV@NG. (b) TEM image and (c) high-angle annular dark-field (HAADF)-STEM image of SAV@NG. (d) HAADF image and corresponding EDS mappings of SAV@NG. (e,f) AC-STEM-ADF images of SAV@NG. (g) NEXAFS N K-edge of g-C_3N_4, NG, Seed-SAV, and SAV@NG. (h) Vanadium K-edge X-ray absorption near edge structure (XANES) spectra of SAV@NG, V foil, VOPc, VO_2, and V_2O_5. (i) Fourier transform of vanadium K-edge EXAFS spectra of SAV@NG, V foil, VOPc, VO_2, and V_2O_5.

nimine (PEI) does not change the basic sp^2 configuration of graphene (Figure S7b). Furthermore, the energy dispersive spectrum (EDS) elemental mapping images indicated that the C, N, and V elements are uniformly distributed throughout the structure (Figure 3c,d). Isolated single atoms were atomically dispersed on the substrate as shown by the aberration-corrected scanning transmission electron microscopy annular dark-field (AC-STEM-ADF) images (Figure 3e and f). Similarly, structural investigation of SACo@NG shows successful synthesis of single cobalt atoms on the surface of graphene (see additional details in Figure S6).

In order to understand the chemical environment of SAV@NG and SACo@NG, low energy X-ray photoelectron spectroscopy (XPS) and high energy X-ray absorption spectroscopy (XAS) were used to analyze the carbon, nitrogen, and vanadium oxidation states (see more detail in Supporting Information). The nitrogen K-edge spectra reveal four characteristic resonances occurring at around 399.2, 400.4, 401.4, and 402.2 eV (Figure 3g), corresponding to aromatic C—N—C coordination in one tri-s-triazine heterosing (N1), terminal C—N—H (N2) bond, graphitic 3-fold nitrogen atom N—3C (N3), and sp^3 N—3C bridging among the three tri-s-triazine moieties (N4), respectively.[33] By comparing with pure

g-C_3N_4 of 399.5 eV, the peak of Seed-SAV shifts to lower energy of 399.0 eV, due to the introduction of V atoms in the g-C_3N_4 structure. The N near edge X-ray absorption fine structure (NEXAFS) indicates Seed-SAV largely maintaining the g-C_3N_4 structure (Figure 3g). In comparison, the SAV@NG and NG show an obvious peak at 398.4 eV, which can be assigned to the pyridinic N,[34] consistent with the XPS results (Figure S8).

In the Seed-SAV, the V form is predominant by V—N and slight low part of V—O, which may be due to the massive N protection in g-C_3N_4. Different from the rigorous inversion symmetry in VO, V_2O_5, and V metal, the pre-edge of SAV@NG shifts to higher energy, suggesting that the coordination symmetry is more distorted (Figure 3h).[35] Turning to XAS, the extended X-ray absorption fine structure (EXAFS) (Figure 3i) profiles indicate the local atomic structure in SAV@NG. The V in SAV@NG shows a lack of V—V bonding (2.24 Å) and is instead dominated by light element bonding, such as V—N (1.30 Å) and V—O (1.56 Å). SAV@NG shows similar structure with that of V in vanadium(IV) oxide phthalocyanine (VOPc), coordinating with two nitrogen atoms and one oxygen. The SAV@NG is dominated by V—N bonding with a smaller V—O contribution and consistent with XPS and
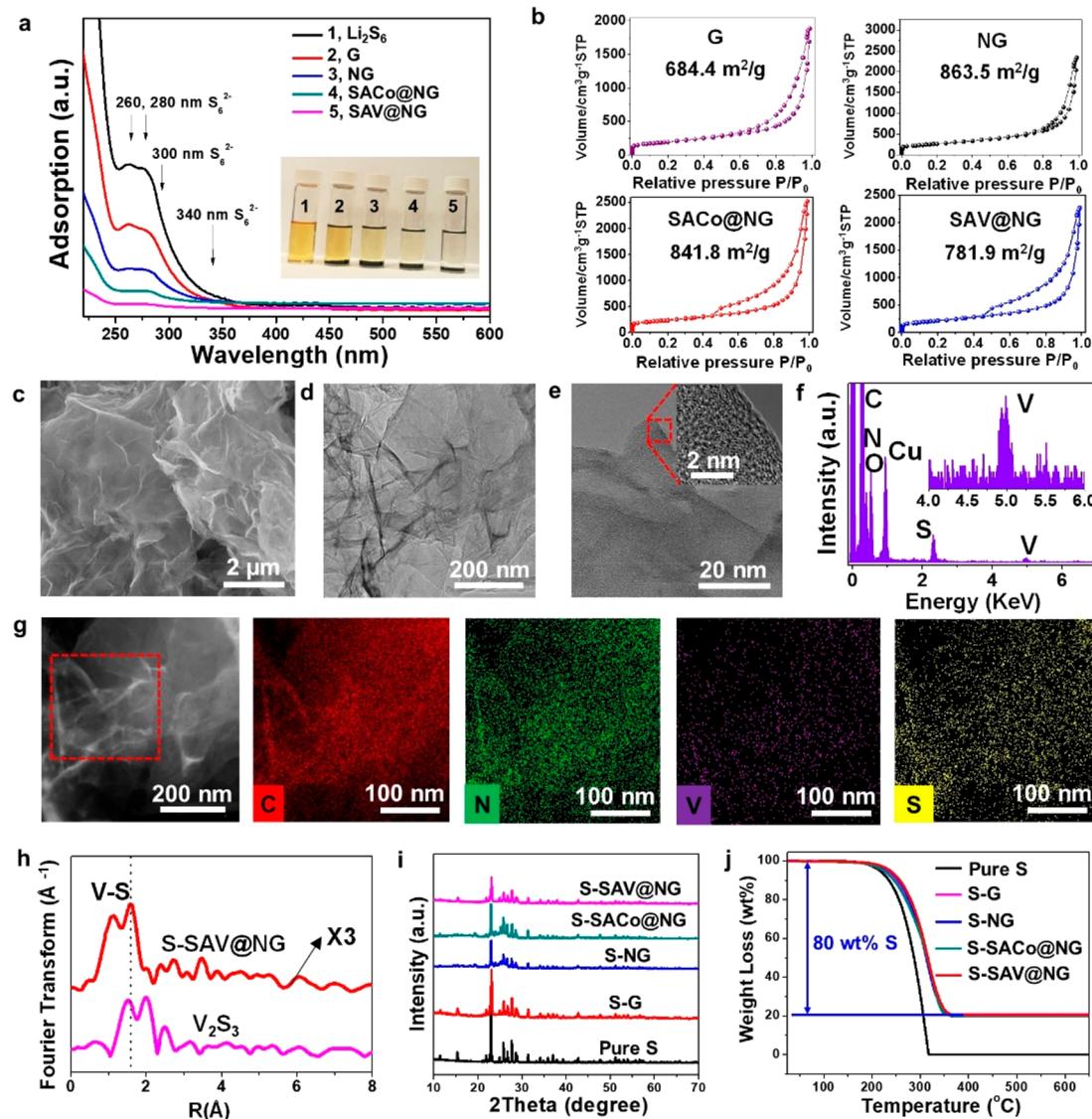
Figure 4. Polysulfide adsorption capability and structural characterizations of S-SAV@NG. (a) UV−vis spectra of the Li_2S_6 solution after exposure to graphene (G), NG, SACo@NG, and SAV@NG and the inserted digital image of Li_2S_6 absorption test in 1,2-dimethoxyethane and 1,3-dioxolane solution (DOL/DME, 1:1 ratio, by volume). (b) Nitrogen adsorption−desorption isotherms of graphene, NG, SACo@NG, and SAV@NG. (c) SEM image of S-SAV@NG. (d) TEM and (e) HRTEM images of S-SAV@NG. (f) EDS spectroscopy of the red plotted area in (g). (g) EDS mappings of S-SAV@NG. (h) Fourier transform of vanadium K-edge EXAFS spectra of S-SAV@NG and V_2S_3. (i) XRD patterns of pure S, S-G, S-NG, S-SACo@NG, and S-SAV@NG. (j) TGA curves of pure S, S-G, S-NG, S-SACo@NG, and S-SAV@NG.

NEXAFS results (Figures S8 and S9). Similarly, the detailed results in Figure S10 reveal that the Co in SACo@NG is also in the form of single atoms.

To understand the LiPSs adsorption capability of these materials, UV−vis absorption spectroscopy was used to compare the concentration change of Li_2S_6 solution after adding graphene, NG, SACo@NG, and SAV@NG (Figure 4a). The characteristic UV−vis peaks of the polysulfide solution located at 260, 280, 300, and 340 nm are assigned to the S_6^{2-} species.[36,37] After the absorption for 1.5 h, it can be obviously observed that the absorption characteristic peaks of Li_2S_6 decrease for both graphene and NG and almost disappear for SACo@NG and SAV@NG (inset of Figure 4a), which confirms better absorption capability for S_6^{2-} in SACo@NG and SAV@NG. Nitrogen adsorption/desorption isotherms were used to obtain the information on porous structure and surface area of the graphene, NG, SACo@, and SAV@NG

samples (Figure 4b), and the results indicate that there is a decrease in specific surface area of SACo@NG (841.8 m^2 g^{-1}) and SAV@NG (781.9 m^2 g^{-1}) compared with NG with a value of 863.5 m^2 g^{-1}, which may be attributed to the added metal that dilutes the value of surface area. The pore size distribution (Figure S11) confirms that sufficient pore structure remained in SACo@NG and SAV@NG. The strong chemical adsorption of SAC with LiPSs and large surface area of the composite are beneficial for constructing high-performance sulfur electrodes in Li−S batteries. Therefore, four electrodes were produced through sulfur infiltration methods. Sulfur is uniformly dispersed on the surface of SAV@NG (S-SAV@NG, Figure 4c) and SACo@NG (S-SACo@NG, Figure S12) without obvious sulfur particle aggregates, which are different from S-G and S-NG (Figure S13). In addition, HRTEM images in Figure 4d,e also confirm the absence of obvious sulfur clusters. The EDS signals at 2.30 and 4.95 keV in Figure 4f indicate the
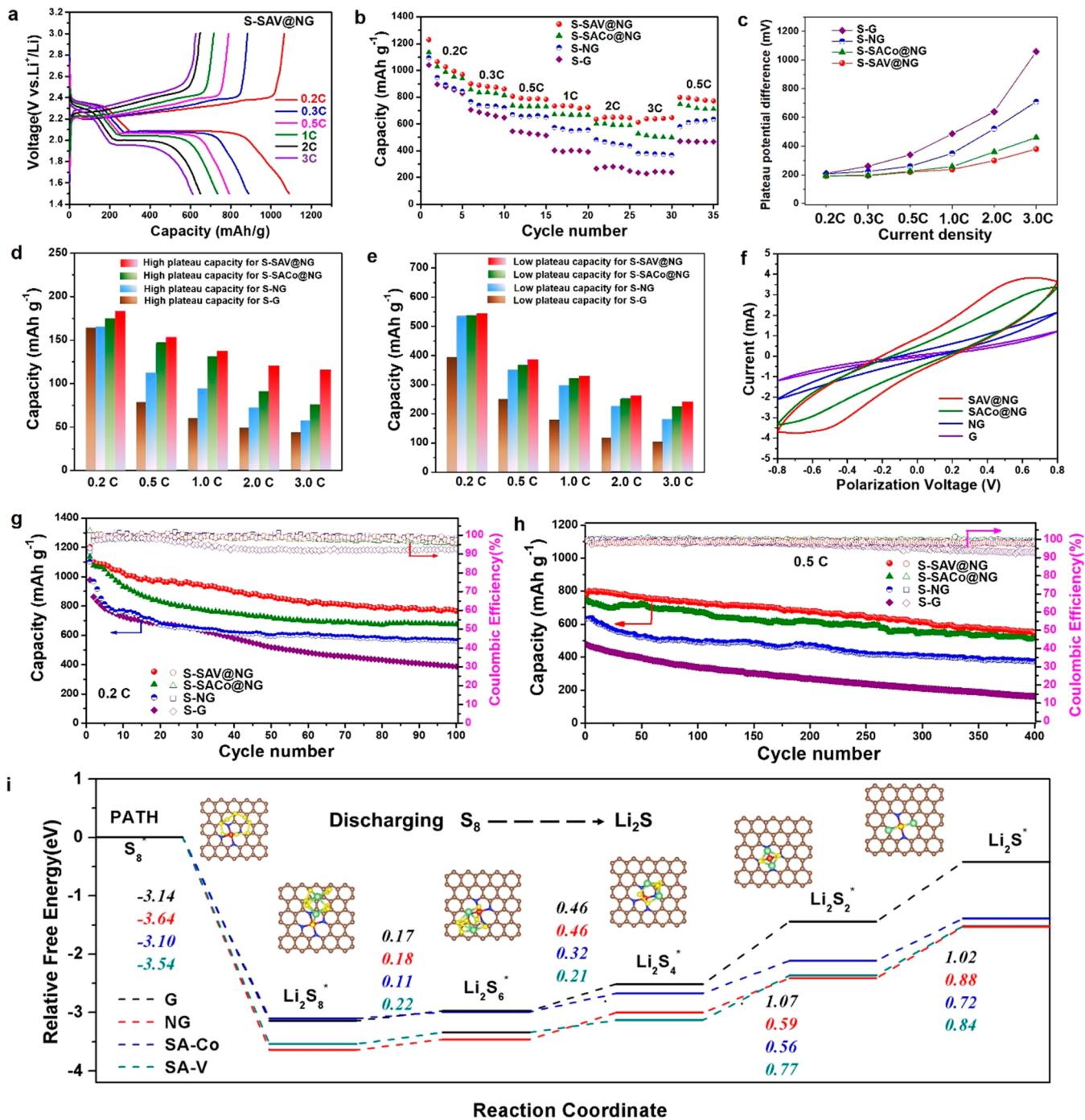
F

Figure 5. Electrochemical performance and mechanism understanding. (a) Charge−discharge voltage profiles of S-SAV@NG electrode at current rates of 0.2, 0.3, 0.5, 1.0, 2.0, and 3.0 C. (b) Rate performance of the S-G, S-NG, S-SACo@NG, and S-SAV@NG electrodes. (c) Comparison of the potential difference between the charge and discharge plateaus at different current densities for the S-G, S-NG, S-SACo@NG, and S-SAV@NG electrodes. (d,e) High and low plateau capacity at different current densities for the S-G, S-NG, S-SACo@NG, and S-SAV@NG electrodes. (f) CV curves of symmetric cells with the S-G, S-NG, S-SACo@NG, and S-SAV@NG electrodes from −0.8 to 0.8 V. (g) Cycling performance and Coulombic efficiency of the S-G, S-NG, S-SACo@NG, and S-SAV@NG electrodes at 0.2 C for 100 cycles. (h) Long-term cycling stability of the S-G, S-NG, S-SACo@NG, and S-SAV@NG electrodes at 0.5 C for 400 cycles. (i) Energy profiles for the reduction of polysulfides on graphene, NG, SACo@NG, and SAV@NG.

presence of S and V in the S-SAV@NG. The uniform elemental distribution of C, N, V, and S reveals the good sulfur dispersion on the SAV@NG (Figure 4g). In addition, the XANES (Figure S14) and EXAFS of S-SAV@NG and V_2S_3 (Figure 4h) were conducted to analyze the V state after sulfur infiltration. The first shell of V−S in V_2S_3 is very close to V−O

around 1.53 Å, with a second shell of about 2.02 Å. It proves that the dextral bonding near to V−S formed in the S-SAV@NG (Figure 4h). XRD patterns of S-G, S-NG, S-SACo@NG, S-SAV@NG, and pristine sulfur exhibit similar characteristic diffraction peaks (Figure 4i), which can be indexed as a typical crystal structure of orthorhombic sulfur (JCPDS No. 08-0247).

TGA is used to determine the sulfur content in the composite and the results indicate a high loading of sulfur in the above-mentioned samples with values up to 80 wt % (Figure 4j). All of these characteristics show great potential for applying single atom seeded graphene in Li−S batteries toward desirable electrochemical performance.

To substantiate the effective S/LiPSs/Li$_2$S catalysis conversion by single atoms in improving the performance of Li−S batteries, a series of electrochemical measurements of S-G, S-NG, S-SACo@NG, and S-SAV@NG electrodes were conducted. From the charge/discharge profiles of the S-SAV@NG electrode (Figure 5a), it is clearly observed that two discharge/charge plateaus are well-retained even at a high rate of 3 C, indicating the excellent reaction kinetics. The S-SAV@NG electrode has an obvious higher discharge plateau at ∼2.32 V (reduction of sulfur to long-chain LiPSs) and a longer plateau at ∼2.10 V (formation of short-chain LiPSs) with corresponding charge plateaus between 2.20 and 2.40 V (transformation from Li$_2$S$_2$/Li$_2$S to long-chain LiPSs and then to sulfur).[38] The efficient catalysis conversion of SAV enables the battery to deliver the highest capacity of 1230 mAh g^{-1} at 0.2 C rate, and the reversible discharge capacity could reach 645 mAh g^{-1} at a high current density of 3 C rate (Figure 5b). When the current rate was abruptly changed back to 0.5 C rate again, the electrode was able to recover to the original capacity, indicating the robustness and stable structure of the S-SAV@NG electrode. Likewise, the S-SACo@NG electrode also exhibits good rate performance with well-defined charge/discharge plateaus, much better than S-G and S-NG electrodes with large polarization especially at high rates (Figure S15). The polarization for the S-SAV@NG and S-SACo@NG electrodes is much lower compared to the S-G and S-NG electrodes at different current densities, for example, the overpotential of S-SAV@NG and S-SACo@NG at 3.0 C is 380 and 460 mV, respectively, much lower than that of S-NG (710 mV) and S-G (1060 mV) electrodes, demonstrating better redox reaction kinetics and good reversibility of single atom seeded sulfur electrodes (Figure 5c). Moreover, the plateaus of the S-SAV@NG electrode are long and flat and are well-retained from 0.3 to 3 C rates between the charge/discharge processes. When comparing the capacity contribution between high and low plateau capacity at different current densities, it is worth noting that the S-SAV@NG has a larger capacity contribution from high and low plateau range especially at high current densities compared with the S-NG and S-SACo@NG electrodes (Figure 5d,e). In sharp contrast, the capacity in high plateau of S-G electrode is only about one-third of SAV@NG electrode at 3 C. Cyclic voltammetry (CV) tests in symmetric cells using an electrolyte containing 0.5 mol L^{-1} Li$_2$S$_6$ and 1 mol L^{-1} LiTFSI dissolved in DOL/DME (v/v = 1/1) were carried out to study the catalytic activity of G, NG, SACo@NG, and SAV@NG electrodes within a potential window from −0.8 to 0.8 V (Figure 5f). The SAV@NG and SACo@NG electrodes exhibit higher current under identical test conditions, indicating rapid polysulfide redox conversion reactions of polysulfides on the electrolyte/electrode surface compared to the other electrodes. The accelerated polysulfide redox reaction kinetics can be ascribed to the catalytic activity of SAV and SACo seeded on the graphene promoting the polysulfide conversion.

The cycling performance of these electrodes was measured at 0.2 C between 1.5 and 2.8 V for 100 cycles, as shown in Figure 5g. The S-SACo@NG and S-SAV@NG electrodes

exhibit good cycling stability with nearly 100% Coulombic efficiency and reversible specific capacities of 675 and 770 mAh g^{-1} after 100 cycles, much higher than those of the S-G and S-NG with values of 388 and 560 mAh g^{-1}, demonstrating the effectiveness of the single atom structural design in confining sulfur species through a combined physical and chemical interaction. In addition, the long-term cyclic test at 0.5 C rate was carried out and the initial specific capacity is 780 and 749 mAh g^{-1} for S-SAV@NG and S-SACo@NG electrodes, respectively, and they stabilized at ∼551 and 513 mAh g^{-1} after 400 cycles, respectively (Figure 5h). The capacity decay is 0.073% and 0.079% per cycle for the S-SAV@NG and S-SACo@NG electrodes, much better than those of S-NG and S-G electrodes with decay rates of 0.101% and 0.165% per cycle, respectively. To further satisfy the requirements of high-energy batteries, the active sulfur loading of S-SAV@NG was increased to 5 mg cm^{-2}. It is obviously observed that the discharging/charging plateaus are still well-retained even at a high rate of 2.0 C (Figure S16a), demonstrating that the reaction kinetic is not influenced by high sulfur loading. The single atom active site catalyst enables the battery to deliver a high initial capacity of 1143 mAh g^{-1} at 0.2 C, and 701, 580, and 430 mAh g^{-1} at higher cycling rates of 0.5, 1.0, and 2.0 C, respectively (Figure S16b). In addition, a long-term cyclic test at 0.5 C rate was conducted and the initial specific capacity is 645 mAh g^{-1}, which stabilizes at ∼485 mAh g^{-1} after 200 cycles (Figure S16c). The significantly improved battery performance can be attributed to the merits of single atom seeded electrode configuration design including (i) the single atom V effectively traps the dissolved LiPSs and provides more active sites for Li$_2$S deposition; (ii) the graphene substrate can improve conductivity of the electrode and accommodate the volume change of the active sulfur and intermediate materials during cycling; (iii) the efficient catalytic conversion of Li$_2$S/LiPSs accelerates the reaction kinetics and prevents the loss of active material, thus realizing a high capacity, fast charging, and long cycling life Li−S battery.

To attain an in-depth understanding of the reasons for the improved discharge reaction kinetics of the S-SACo@NG and S-SAV@NG cathodes, the overall reactions based on the reversible formation of Li$_2$S from S$_8$ and Li bulk were considered as shown in Figure 5i. The Gibbs free energies for all of the reaction steps were calculated and the evolution profile from S$_8$ to Li$_2$S species on all the substrates are exhibited. The detailed optimized structures of the intermediates on the SAV@NG substrate were shown in the inset, while other atomic configurations can be seen in Figure S17. It can be seen that the reduction step of S$_8$ to the Li$_2$S$_8$ shows a spontaneous exothermic reaction on all the substrates. The following four reduction steps, from Li$_2$S$_6$ to Li$_2$S, were an endothermic reaction, while the last two steps from Li$_2$S$_4$ to Li$_2$S$_2$ and Li$_2$S$_2$ to Li$_2$S exhibit the big positive Gibbs energy barrier comparing to other steps. The rate-limiting step in the graphene is the step from Li$_2$S$_4$ to Li$_2$S$_2$ with the value of 1.07 eV, but the rate-limiting step for the NG, SACo@NG, and SAV@NG is the step from Li$_2$S$_2$ to the Li$_2$S. Considering the low positive Gibbs energy barrier of rate-limiting step on SACo@NG (0.72 eV) and SAV@NG (0.84 eV), the reduction process of sulfur is more convenient on these substrates during discharging and thus improves the electrochemical performance of Li−S batteries.

In summary, we have demonstrated a well-characterized and customizable method to synthesize SACs supported on

graphene via a seeding strategy with scalable amount, controllable loading, and adjustable components. On the basis of the guidance of theoretical simulations, vanadium atom catalysts were chosen and prepared for high-performance Li−S batteries. The great improvement in the battery capacity, kinetics, and cycling life confirms the merits of SACs. The single vanadium active catalysis sites facilitate both the formation and decomposition of solid Li_2S in discharging and charging processes, which guarantee a high utilization of sulfur species. The precise synthesis of commercial quantities of SACs directly guided by theoretical calculations and our seeding fabrication approach provide tremendous opportunities for developing high energy/power density and long-life rechargeable batteries.

■ ASSOCIATED CONTENT

ⓢ Supporting Information

The Supporting Information is available free of charge at https://pubs.acs.org/doi/10.1021/acs.nanolett.9b04719.

> Methods, additional figures, and additional references (PDF)

■ AUTHOR INFORMATION

Corresponding Authors
*E-mail: s.jiang@curtin.edu.au,
*E-mail: qianfan@buaa.edu.cn,
*E-mail: yicui@stanford.edu.

ORCID ⃝
Guangmin Zhou: 0000-0002-3629-5686
Shi-Ze Yang: 0000-0002-0421-006X
Hao Chen: 0000-0002-2852-0070
Yusheng Ye: 0000-0001-9832-2478
Yecun Wu: 0000-0001-6011-4489
San Ping Jiang: 0000-0002-7042-2976
Qianfan Zhang: 0000-0001-8121-7727
Yi Cui: 0000-0002-6103-6352

Author Contributions
◆G.Z., S.Z., and T.W. contributed equally to this work

Author Contributions
G.Z., S.Z., Q.Z., and Y.C. conceived the concept and experiments. G.Z. and S.Z. prepared samples, built the cells, and carried out experiment characterizations. T.W. and Q.Z. carried out the DFT calculations. S.Y. and B.J. assisted in material characterization. H.C., C.L., Y.Y., Y.W., and Y.P. assisted in the device fabrication and electrochemical measurements. C.L. and S.J. participated in discussions. G.Z., S.Z., T.W., Q.Z., and Y.C. analyzed data and wrote the paper. All authors discussed the results and commented on the manuscript.

Notes
The authors declare no competing financial interest.

■ ACKNOWLEDGMENTS

■ REFERENCES

(1) Bruce, P. G.; Freunberger, S. A.; Hardwick, L. J.; Tarascon, J.-M. Li-O₂ and Li-S Batteries with High Energy Storage. *Nat. Mater.* **2012**, *11*, 19−29.

(2) Pang, Q.; Liang, X.; Kwok, C. Y.; Nazar, L. F. Advances in Lithium−Sulfur Batteries Based on Multifunctional Cathodes and Electrolytes. *Nat. Energy* **2016**, *1*, 16132.

(3) Liu, Y.; Zhou, G.; Liu, K.; Cui, Y. Design of Complex Nanomaterials for Energy Storage: Past Success and Future Opportunity. *Acc. Chem. Res.* **2017**, *50*, 2895−2905.

(4) Manthiram, A.; Fu, Y.; Chung, S.-H.; Zu, C.; Su, Y.-S. Rechargeable Lithium−Sulfur Batteries. *Chem. Rev.* **2014**, *114*, 11751−11787.

(5) Zhou, G.; Xu, L.; Hu, G.; Mai, L.; Cui, Y. Nanowires for Electrochemical Energy Storage. *Chem. Rev.* **2019**, *119*, 11042−11109.

(6) Yun, J. H.; Kim, J.-H.; Kim, D. K.; Lee, H.-W. Suppressing Polysulfide Dissolution Via Cohesive Forces by Interwoven Carbon Nanofibers for High-Areal-Capacity Lithium−Sulfur Batteries. *Nano Lett.* **2018**, *18*, 475−481.

(7) Yuan, Z.; Peng, H.-J.; Hou, T.-Z.; Huang, J.-Q.; Chen, C.-M.; Wang, D.-W.; Cheng, X.-B.; Wei, F.; Zhang, Q. Powering Lithium−Sulfur Battery Performance by Propelling Polysulfide Redox at Sulfiphilic Hosts. *Nano Lett.* **2016**, *16*, 519−527.

(8) Liu, D.; Zhang, C.; Zhou, G.; Lv, W.; Ling, G.; Zhi, L.; Yang, Q.-H. Catalytic Effects in Lithium−Sulfur Batteries: Promoted Sulfur Transformation and Reduced Shuttle Effect. *Adv. Sci.* **2018**, *5*, 1700270.

(9) Zhou, G. M.; Zhao, Y.; Zu, C.; Manthiram, A. Free-Standing TiO₂ Nanowire-Embedded Graphene Hybrid Membrane for Advanced Li/Dissolved Polysulfide Batteries. *Nano Energy* **2015**, *12*, 240−249.

(10) Wang, Y.; Zhang, R.; Chen, J.; Wu, H.; Lu, S.; Wang, K.; Li, H.; Harris, C. J.; Xi, K.; Kumar, R. V.; et al. Enhancing Catalytic Activity of Titanium Oxide in Lithium−Sulfur Batteries by Band Engineering. *Adv. Energy Mater.* **2019**, *9*, 1900953.

(11) Zhou, G.; Tian, H.; Jin, Y.; Tao, X.; Liu, B.; Zhang, R.; Seh, Z. W.; Zhuo, D.; Liu, Y.; Sun, J.; et al. Catalytic Oxidation of Li₂s on the Surface of Metal Sulfides for Li−S Batteries. *Proc. Natl. Acad. Sci. U. S. A.* **2017**, *114*, 840−845.

(12) Liang, X.; Hart, C.; Pang, Q.; Garsuch, A.; Weiss, T.; Nazar, L. F. A Highly Efficient Polysulfide Mediator for Lithium−Sulfur Batteries. *Nat. Commun.* **2015**, *6*, 5682.

(13) Zheng, C.; Niu, S.; Lv, W.; Zhou, G.; Li, J.; Fan, S.; Deng, Y.; Pan, Z.; Li, B.; Kang, F.; et al. Propelling Polysulfides Transformation

for High-Rate and Long-Life Lithium—Sulfur Batteries. *Nano Energy* **2017**, *33*, 306−312.

(14) Wang, Y.; Zhang, R.; Pang, Y.-c.; Chen, X.; Lang, J.; Xu, J.; Xiao, C.; Li, H.; Xi, K.; Ding, S. Carbon@Titanium Nitride dual Shell Nanospheres as Multi-Functional Hosts for Lithium Sulfur Batteries. *Energy Storage Mater.* **2019**, *16*, 228−235.

(15) Yang, X.; Gao, X.; Sun, Q.; Jand, S. P.; Yu, Y.; Zhao, Y.; Li, X.; Adair, K.; Kuo, L.-Y.; Rohrer, J.; et al. Promoting the Transformation of Li$_2$S$_2$ to Li$_2$S: Significantly Increasing Utilization of Active Materials for High-Sulfur-Loading Li—S Batteries. *Adv. Mater.* **2019**, *31*, 1901220.

(16) Sun, Z.; Zhang, J.; Yin, L.; Hu, G.; Fang, R.; Cheng, H.-M.; Li, F. Conductive Porous Vanadium Nitride/Graphene Composite as Chemical Anchor of Polysulfides for Lithium-Sulfur Batteries. *Nat. Commun.* **2017**, *8*, 14627.

(17) Li, L.; Chen, L.; Mukherjee, S.; Gao, J.; Sun, H.; Liu, Z.; Ma, X.; Gupta, T.; Singh, C. V.; Ren, W.; et al. Phosphorene as a Polysulfide Immobilizer and Catalyst in High-Performance Lithium—Sulfur Batteries. *Adv. Mater.* **2017**, *29*, 1602734.

(18) Yang, X.-F.; Wang, A.; Qiao, B.; Li, J.; Liu, J.; Zhang, T. Single-Atom Catalysts: A New Frontier in Heterogeneous Catalysis. *Acc. Chem. Res.* **2013**, *46*, 1740−1748.

(19) Liu, J. Catalysis by Supported Single Metal Atoms. *ACS Catal.* **2017**, *7*, 34−59.

(20) Qiao, B.; Wang, A.; Yang, X.; Allard, L. F.; Jiang, Z.; Cui, Y.; Liu, J.; Li, J.; Zhang, T. Single-Atom Catalysis of Co Oxidation Using Pt$_1$/FeO$_x$. *Nat. Chem.* **2011**, *3*, 634−641.

(21) Zhu, C.; Fu, S.; Shi, Q.; Du, D.; Lin, Y. Single-Atom Electrocatalysts. *Angew. Chem., Int. Ed.* **2017**, *56*, 13944−13960.

(22) Wang, A.; Li, J.; Zhang, T. Heterogeneous Single-Atom Catalysis. *Nat. Rev. Mater.* **2018**, *2*, 65−81.

(23) Xu, H.; Cheng, D.; Cao, D.; Zeng, X. C. A Universal Principle for a Rational Design of Single-Atom Electrocatalysts. *Nat. Catal.* **2018**, *1*, 339−348.

(24) Kyriakou, G.; Boucher, M. B.; Jewell, A. D.; Lewis, E. A.; Lawton, T. J.; Baber, A. E.; Tierney, H. L.; Flytzani-Stephanopoulos, M.; Sykes, E. C. Isolated Metal Atom Geometries as a Strategy for Selective Heterogeneous Hydrogenations. *Science* **2012**, *335*, 1209.

(25) Wang, J.; Jia, L.; Zhong, J.; Xiao, Q.; Wang, C.; Zang, K.; Liu, H.; Zheng, H.; Luo, J.; Yang, J.; et al. Single-Atom Catalyst Boosts Electrochemical Conversion Reactions in Batteries. *Energy Storage Mater.* **2019**, *18*, 246−252.

(26) Du, Z.; Chen, X.; Hu, W.; Chuang, C.; Xie, S.; Hu, A.; Yan, W.; Kong, X.; Wu, X.; Ji, H.; et al. Cobalt in Nitrogen-Doped Graphene as Single-Atom Catalyst for High-Sulfur Content Lithium—Sulfur Batteries. *J. Am. Chem. Soc.* **2019**, *141*, 3977−3985.

(27) Xie, J.; Li, B.-Q.; Peng, H.-J.; Song, Y.-W.; Zhao, M.; Chen, X.; Zhang, Q.; Huang, J.-Q. Implanting Atomic Cobalt within Mesoporous Carbon toward Highly Stable Lithium—Sulfur Batteries. *Adv. Mater.* **2019**, *31*, 1903813.

(28) Zhang, L.; Liu, D.; Muhammad, Z.; Wan, F.; Xie, W.; Wang, Y.; Song, L.; Niu, Z.; Chen, J. Single Nickel Atoms on Nitrogen-Doped Graphene Enabling Enhanced Kinetics of Lithium—Sulfur Batteries. *Adv. Mater.* **2019**, *31*, 1903955.

(29) Urban, A.; Seo, D.-H.; Ceder, G. Computational Understanding of Li-Ion Batteries. *Npj Comput. Mater.* **2016**, *2*, 16002.

(30) Chen, X.; Peng, H.-J.; Zhang, R.; Hou, T.-Z.; Huang, J.-Q.; Li, B.; Zhang, Q. An Analogous Periodic Law for Strong Anchoring of Polysulfides on Polar Hosts in Lithium Sulfur Batteries: S- or Li-Binding on First-Row Transition-Metal Sulfides? *ACS Energy Lett.* **2017**, *2*, 795−801.

(31) Zhao, S.; Chen, G.; Zhou, G.; Yin, L.-C.; Veder, J.-P.; Johannessen, B.; Saunders, M.; Yang, S.-Z.; De Marco, R.; Liu, C.; et al. A Universal Seeding Strategy to Synthesis Single Atom Catalysts on 2D Materials for Electrocatalytic Applications. *Adv. Funct. Mater.* **2019**, 1906157.

(32) Zhang, Q.; Wang, Y.; Seh, Z. W.; Fu, Z.; Zhang, R.; Cui, Y. Understanding the Anchoring Effect of Two-Dimensional Layered Materials for Lithium—Sulfur Batteries. *Nano Lett.* **2015**, *15*, 3780−3786.

(33) Lakhi, K. S.; Park, D.-H.; Singh, G.; Talapaneni, S. N.; Ravon, U.; Al-Bahily, K.; Vinu, A. Energy Efficient Synthesis of Highly Ordered Mesoporous Carbon Nitrides with Uniform Rods and Their Superior CO$_2$ Adsorption Capacity. *J. Mater. Chem. A* **2017**, *5*, 16220−16230.

(34) Yang, H. B.; Miao, J.; Hung, S.-F.; Chen, J.; Tao, H. B.; Wang, X.; Zhang, L.; Chen, R.; Gao, J.; Chen, H. M.; et al. Identification of Catalytic Sites for Oxygen Reduction and Oxygen Evolution in N-Doped Graphene Materials: Development of Highly Efficient Metal-Free Bifunctional Electrocatalyst. *Sci. Adv.* **2016**, *2*, No. e1501122.

(35) Haskel, D.; Islam, Z.; Lang, J.; Kmety, C.; Srajer, G.; Pokhodnya, K. I.; Epstein, A. J.; Miller, J. S. Local Structural Order in the Disordered Vanadium Tetracyanoethylene Room-Temperature Molecule-Based Magnet. *Phys. Rev. B: Condens. Matter Mater. Phys.* **2004**, *70*, 054422.

(36) Barchasz, C.; Molton, F.; Duboc, C.; Lepretre, J. C.; Patoux, S.; Alloin, F. Lithium/Sulfur Cell Discharge Mechanism: An Original Approach for Intermediate Species Identification. *Anal. Chem.* **2012**, *84*, 3973−3980.

(37) Zhou, G. M.; Paek, E.; Hwang, G. S.; Manthiram, A. Long-Life Li/Polysulphide Batteries with High Sulphur Loading Enabled by Lightweight Three-Dimensional Nitrogen/Sulphur-Codoped Graphene Sponge. *Nat. Commun.* **2015**, *6*, 7760−7770.

(38) Zhou, G. M.; Pei, S.; Li, L.; Wang, D.-W.; Wang, S.; Huang, K.; Yin, L.-C.; Li, F.; Cheng, H.-M. A Graphene—Pure-Sulfur Sandwich Structure for Ultrafast, Long-Life Lithium—Sulfur Batteries. *Adv. Mater.* **2014**, *26*, 625−631.